Chapter 3

Side-Coupled Array of Qubits

In this chapter we have studied a more commonly realized model, namely an array of resonators to which qubits are side-coupled. Examples of realization include an array of cavities with an atom inside each cavity or the superconducting circuit analog of this system. The physical system investigated in Fitzpatrick et al. [2017] also corresponds to a chain of connected resonators to each of which a qubit is side-coupled. In contrast to Fitzpatrick et al. [2017], we consider here no photon loss from the resonators in the one-dimensional open QED medium.

3.1 Model

The model and techniques discussed in previous chapter generalize in a straightforward manner to the system of side-coupled qubits, for which the medium Hamiltonian, Eq. 2.1, is given by

$$H_M = H_{side} = \sum_{j=1}^{N} (H_j^q + H_j^r + H_j^{rq}) + \sum_{j=1}^{N-1} H_j^{hop}, \tag{3.1}$$

where,

$$\begin{aligned} H_j^q &= \hbar\omega_{q_j} b_j^\dagger b_j + \hbar U b_j^\dagger b_j (b_j^\dagger b_j - 1), \\ H_j^r &= \hbar\omega_{r_j} f_j^\dagger f_j, \qquad H_j^{rq} = \hbar g_j (b_j^\dagger f_j + f_j^\dagger b_j), \\ H_j^{hop} &= 2\hbar J_x (f_j^\dagger f_{j+1} + f_{j+1}^\dagger f_j). \end{aligned}$$

Similar to the directly coupled qubit chain, $b_j^\dagger$ and b_j are the creation and annihilation operators for the qubits with qubit frequency ω_{q_j} and on-site interaction U. The resonator chain is a 1D array of bosonic resonators with creation and annihilation operators $f_j^\dagger$ and f_j, respectively, and resonator frequency ω_{r_j}. Each resonator in the chain is coupled to its nearest neighbors, with coupling strength $2J_x$, and side-coupled with the qubit, with resonator-qubit coupling strength g_j. The side-coupled medium is coupled to the two baths through $\chi_1 = f_1$ and $\chi_N = f_N$.

3.2 Analysis

The analysis of this system requires a few additional steps compared to the previous chapter which we discuss below.

3.2.1 Truncated Heisenberg-Langevin equations

As the qubits (resonators) are bosonic, each of them can have any number of excitations. These excited states appear as powers of b_j and $b_j^\dagger$ (f_j and $f_j^\dagger$) in the operators. To describe the THLE, we need to consider every independent boson operator for each qubit /resonator for each site similar to the direct-coupled array of qubits.

3.2.2 Integrating out the resonators

To model the side-coupled system of qubits, we first solve the equations for the resonators coupled to the baths and qubits, just as it was done in the case of baths. For a single qubit-resonator pair, we denote the expectation values of resonator operators after integrating the baths similar to those of the qubits in Eq. 2.10 by:

$$F_{kl}(t) = \langle f_1^{\dagger k} f_1^l \rangle e^{(-k+l)i\omega_p(t-t_0)}. \tag{3.2}$$

With this notation, the equation for the resonator variable becomes

$$\dot{F}_{01}(t) = -(i\delta\omega_{r_1} + \Gamma)F_{01}(t) - ig_1\mathscr{S}_{01}(t) - i\Omega_L. \tag{3.3}$$

Here, $\delta\omega_{r_1} = \omega_{r_1} - \omega_p$, $\Gamma = \Gamma_L + \Gamma_R$ and $\mathscr{S}_{01}(t)$ is the qubit operator as mentioned in Sec. 2.3.1. Since the resonator has no non-linearity (it is modeled as a harmonic oscillator), we note that Eq. 3.3 is an inhomogeneous linear differential equation which is not connected to any other variables of the resonator apart from F_{01}. We now integrate Eq. 3.3 to obtain a

formal solution of the equation as:

$$F_{01}(t) = F_{01}(t_0)\mathscr{G}_A(t-t_0) - i\Omega_L \int_{t_0}^{t} \mathscr{G}_A(t-t')dt' - ig_1 \int_{t_0}^{t} \mathscr{G}_A(t-t')\mathscr{S}_{01}(t')dt', \tag{3.4}$$

where, $\mathscr{G}_A(\tau) = e^{-A\tau}\theta(\tau)$ and $A = i\delta\omega_{r_1} + \Gamma$. This is quite analogous to integrating out the baths, except that the last integral in Eq. 3.4 retains a memory of the qubits' time-evolution; thus, the Eq. 3.4 is non-Markovian in nature. For simplicity, we now make the Markovian approximation, and we replace $\mathscr{S}_{01}(t')$ in Eq. 3.4 by $\mathscr{S}_{01}(t)$. This simplifies the equation by neglecting any retardation effect. We can now write at long-time $(t \to \infty)$ steady-state:

$$F_{01}(t \to \infty) = -i\Omega_L/A - ig_1\mathscr{S}_{01}(t \to \infty)/A. \tag{3.5}$$

The Eq. 3.5 is then substituted in the differential equations obtained after taking expectation of the equations of the qubits, which for m=2 at long time $(t \to \infty)$ gives

$$\begin{aligned}
\dot{\mathscr{S}}_{01}(\infty) &= -\left[i\delta\omega_{q_1} + g_1^2/A\right]\mathscr{S}_{01} - 2iU\mathscr{S}_{12} - g_1\Omega_L/A, && (3.6)\\
\dot{\mathscr{S}}_{02}(\infty) &= -2\left[i\delta\omega_{q_1} + g_1^2/A\right]\mathscr{S}_{02} - 2iU(\mathscr{S}_{02} + 2\mathscr{S}_{13}) - 2g_1\Omega_L\mathscr{S}_{01}/A, && (3.7)\\
\dot{\mathscr{S}}_{11}(\infty) &= -\left[g_1^2/A + g_1^2/A^*\right]\mathscr{S}_{11} - g_1\Omega_L\mathscr{S}_{10}/A - g_1\Omega_L\mathscr{S}_{01}/A^*, && (3.8)\\
\dot{\mathscr{S}}_{12}(\infty) &= -\left[i\delta\omega_{q_1} + 2g_1^2/A + g_1^2/A^*\right]\mathscr{S}_{12} - 2iU(\mathscr{S}_{12} + 2\mathscr{S}_{23}) - g_1\Omega_L 2\mathscr{S}_{11}/A \\
&\quad -g_1\Omega_L\mathscr{S}_{02}/A^*, && (3.9)\\
\dot{\mathscr{S}}_{22}(\infty) &= -2\left[g_1^2/A + g_1^2/A^*\right]\mathscr{S}_{22} - 2g_1\Omega_L\mathscr{S}_{21}/A - 2g_1\Omega_L\mathscr{S}_{12}/A^*, && (3.10)
\end{aligned}$$

and the rest of the equations are hermitian conjugates of 3.6, 3.7, 3.9. The Eqs. 3.6-3.10 and its hermitian conjugates can be re-written in the matrix form and solved to obtain the steady-state solution in the same way as mentioned in Sec. 2.3.1.

For longer system lengths, similar to the system of single qubit-resonator pair, we obtain N linear inhomogeneous equations for the resonators in an array of N resonator-qubit pairs. Also similar to the single site case, the above mentioned approximations can be applied to integrate the resonators' equations and to obtain the long-time steady-state relations between F's and $\mathscr{S}$'s. After integration, the steady-state relations between F's and $\mathscr{S}$'s are in turn substituted in the differential equations obtained after taking expectation of the equations of the qubits. As the resonators can be integrated out, the numerical complexity of the problem is determined only by the qubits.

3.2.3 The quasi-classical analysis

The quasi-classical equations can be derived for the side-coupled qubits in the same manner as it was for the case for direct-coupled array of qubits. For the resonator chain, let $\langle f_j \rangle = \alpha_j$ and hence for N resonator-qubit pairs in the side-coupled model we get $2N$ quasi-classical equations which are

$$\dot{\alpha_j} = -(i\delta\omega_{r_j} + \Gamma_j)\alpha_j - 2iJ_x(\alpha_{j-1} + \alpha_{j+1}), -ig_j\beta_j - i\Omega_L\delta_{1,j} \tag{3.11}$$

$$\dot{\beta_j} = -i\delta\omega_{q_j}\beta_j - 2iU|\beta_j|^2\beta_j - ig_j\alpha_j, \tag{3.12}$$

where, $\Gamma_j = 0$ for $2 \leq j \leq N-1$, $\Gamma_1 = \Gamma_L$ and $\Gamma_N = \Gamma_R$. If $N = 1$, $\Gamma = \Gamma_L + \Gamma_R$. Again we use the open boundary condition, i.e. $\alpha_0 = \alpha_{N+1} = 0$. Rest of the details are again same as it was for direct-coupled array of qubits.

3.2.4 Modified quasi-classical equations

The development for this section will follow the same procedure as of direct-coupled array of qubits case. The correction for the on-site interaction can also be carried out for the more realistic side-coupled system. Again, for the side-coupled system, we try to replicate the THLE results using the QCA and obtain a similar expression for U_{eff}. For a single qubit-resonator pair, the complex on-site interaction also nicely captures the inelastic scattering of the photons and related reduction in transmission.

To calculate the complex on-site interaction (U_{eff}) for the side-coupled qubits medium, we match the transmission probabilities of the THLE and the QCA for a single resonator-qubit pair. To calculate the steady-state solutions of the THLE, we consider a truncated set of the operators $S^T = \begin{bmatrix} S_{01} & \overline{S_{01}} & S_{11} & S_{12} & \overline{S_{12}} & S_{02} & \overline{S_{02}} \end{bmatrix}$. The THLEs for these operators are given by Eqs. 3.6-3.9 and their conjugates. In contrast to direct-coupled qubits case, we require a larger operator set to calculate U_{eff} in order to perfectly match the modified QCA results with those from the THLE analysis.

After solving the set of seven coupled THLEs, we obtain the expected steady-state solution for $\mathscr{S}_{01}^{\infty}$ in terms of $\mathscr{S}_{11}^{\infty}$ as

$$\mathscr{S}_{01}^{\infty} = E_1 + E_2\mathscr{S}_{11}^{\infty}, \tag{3.13}$$

and the expectation value of $\mathscr{S}_{11}^{\infty}$ is given as

$$\mathscr{S}_{11}^{\infty} = \frac{-\Omega_L(A^*E_1^* + AE_1)}{g_1(A + A^*) + \Omega_L(AE_2 + A^*E_2^*)}, \tag{3.14}$$

where,

$$E_1 = \frac{-g_1\Omega_L(i\delta\omega_{q_1}AA^* + 2g_1^2A^* + g_1A + 2iUAA^*)(i\delta\omega_{q_1}A + g_1^2 + iUA)(i\delta\omega_{q_1}A + g_1^2)AA^*}{(i\delta\omega_{q_1}A + g_1^2)\Big((D1)(D2)(D3) + 2iUg_1^2\Omega_L^2A^2\Big)}, \tag{3.15}$$

$$E_2 = \frac{4iUg_1\Omega_L(i\delta\omega_{q_1}A + g_1^2 + iUA)A^*}{(D1)(D2)(D3)AA^* + 2iUg_1^2\Omega_L^2A}, \tag{3.16}$$

where, $D1 = (i\delta\omega_{q_1}AA^* + 2g_1^2A^* + g_1A + 2iUAA^*)$, $D2 = (i\delta\omega_{q_1}A + g_1^2 + iUA)$, $D3 = (i\delta\omega_{q_1}A + g_1^2)$, and $A = i\delta\omega_{r_1} + \Gamma$ and $\Gamma = \Gamma_L + \Gamma_R$. By integrating out the resonators we have obtained the expected value F_{01}^{∞} in Eq. 3.5

The quasi-classical equations for the side-coupled medium at steady-state for $N = 1$ are

$$(i\delta\omega_{r_1} + \Gamma)\alpha_1^{ss} + ig_1\beta_1^{ss} + i\Omega_L = 0, \tag{3.17}$$

$$i\delta\omega_{q_1}\beta_1^{ss} + 2iU|\beta_1^{ss}|^2\beta_1^{ss} + ig_1\alpha_1^{ss} = 0. \tag{3.18}$$

The transmission probabilities for the THLE and QCA for $N = 1$ at steady-state is given by

$$\mathscr{T}_{\text{THLE}} = \frac{2\Gamma_R}{v_g I_{\text{in}}}F_{11}^{\infty}, \tag{3.19}$$

$$\mathscr{T}_{\text{QCA}} = \frac{2\Gamma_R}{v_g I_{\text{in}}}|\alpha_1^{ss}|^2, \tag{3.20}$$

where F_{11}^{∞} is given by Eq. 3.24. Similar to direct-coupled medium's case, we match the steady-state THLE and QCA transmission probabilities by demanding $|\alpha_1^{ss}|^2 = F_{11}^{\infty}$. Again, we choose the phase of α_1^{ss} to be the same as F_{01}^{∞} which gives α_1^{ss} as

$$\alpha_1^{ss} = \frac{\sqrt{F_{11}^{\infty}}F_{01}^{\infty}}{|F_{01}^{\infty}|}. \tag{3.21}$$

The Eq. 3.17 also gives us the expression for β_1^{ss} which is $\beta_1^{ss} = -(\Omega_L + (\delta\omega_{r_1} - i\Gamma)\alpha_1^{ss})/g_1$. Finally, we replace U with U_{eff} in Eq. 3.18 and solve for U_{eff} which is given by

$$U_{\text{eff}} = -\frac{\delta\omega_{q_1}\beta_1^{ss} + g_1\alpha_1^{ss}}{2|\beta_1^{ss}|^2\beta_1^{ss}}. \tag{3.22}$$

The transmission probability even for a single qubit-resonator pair, given by Eqs. 3.19, 3.24, 3.13-3.16, is a very long cumbersome expression analytically. However, several features of this system are present even at low intensity which can be captured by single-particle calculation presented in subsection 3.3.3.

3.2.5 Transmission probability for the medium

For the side-coupled qubits, the output photons are coming out from the resonator at the rightmost end and not from the qubit as for the direct-coupled qubit system. Hence, for a medium of N qubit-resonators pairs, the transmission probability is given as

$$\mathscr{T}_{\mathrm{THLE}}(t) = \frac{2\Gamma_R}{v_g I_{\mathrm{in}}} \langle f_N^\dagger f_N \rangle, \tag{3.23}$$

where $\langle f_N^\dagger f_N \rangle$ is the expectation value of the number operator of the rightmost resonator. It is found by substituting the steady-state solutions of the qubits' variables in the integrated output resonator's equation at steady-state. For example, for a single qubit-resonator pair, to find the resonator number operator (F_{11}), we multiply Eq. 3.5 with its conjugate, to obtain the final relation as

$$F_{11} = \frac{\Omega_L^2 + g_1 \Omega_L (\mathscr{S}_{01} + \mathscr{S}_{10}) + g_1^2 \mathscr{S}_{11}}{AA^*}. \tag{3.24}$$

Longer system sizes can also be dealt in a similar manner. Similar to Eq. 2.30, we can obtain the transmission probability for the side-coupled array of qubits using the quasi-classical equations as

$$\mathscr{T}_{\mathrm{QCA}}(t) = \frac{2\Gamma_R}{v_g I_{\mathrm{in}}} \alpha_N^*(t) \alpha_N(t). \tag{3.25}$$

The reflection probability in the THLE is given by

$$\mathscr{R}_{\mathrm{THLE}}(t) = 1 + \frac{2\Omega_L}{v_g I_{\mathrm{in}}} Im[\langle \chi_1 \rangle] + \frac{2\Gamma_L}{v_g I_{\mathrm{in}}} \langle \chi_1^\dagger \chi_1 \rangle, \tag{3.26}$$

where χ_1 is f_1 for the side-coupled qubits medium. We have explicitly verified numerically that $\mathscr{T}^{\infty}_{\mathrm{THLE}} + \mathscr{R}^{\infty}_{\mathrm{THLE}} = 1$ (Fig. 3.6).

3.3 Results

For THLE we solve the system of qubits equations, with resonators equation integrated out, to obtain the transmission from the right end of the medium. We assume all the qubits and resonators to be in their ground state and set $v_g = 1$. Unlike the direct-coupled case, we observe a reduction of photon transport due to effective photon-photon interactions only at intermediate intensities for the side-coupled system. At very large intensities, the side-coupled system starts to behave more like a resonator chain without any qubits. This is because the qubits get saturated by the photons and are no longer able to create effective

photon-photon interactions blocking the photon transport through the resonator, which results in recovery of photon transport at a high intensity.

We show the transmission results for the medium of one qubit-resonator pair coupled to the baths in Fig. 3.1. The two columns in the figure correspond to two different qubit-resonator coupling strengths (g_1), which are $g_1 = 0.02\omega_a$ on the left and $g_1 = 0.05\omega_a$ on the right. The basic features of the side-coupled qubits' transmission profile at low intensity can be seen in Fig. 3.1(a,b), where we observe two transmission peaks with perfect resonant photon transport separated by a large valley with a minima in transmission at $\omega_p = \omega_a$. We have chosen the resonator (ω_{r_1}) and qubit (ω_{q_1}) frequencies to be equal in Fig. 3.1, however, when resonator and qubit frequencies are not equal, the minima in transmission occurs whenever ω_p is equal to the qubit frequency. The maxima in transmission at low intensities of incident light are near the resonance frequencies (or normal modes) of the isolated medium, and the minima in between the two resonance frequencies is due to destructive interference (subsection 3.3.3). The effect of increasing g_1, at low intensity, can be seen in Fig. 3.1(b) where the two peaks have now moved further apart and the dip between them has become broader, which suggests an increased influence of the qubit in the medium.

In the first four rows, I_{in} gradually increases on going down the columns. The THLE analysis shows that the increase in intensity initially causes disruption of photon transport and the transmission peaks to lower down, Fig. 3.1(c)-(h), which is similar to lowering of transmission observed in the direct-coupled qubits system. The reduction in transmission is again due to the effective photon-photon interactions at higher intensities mediated by the on-site interaction present in the qubits. Such effective interactions block the propagation of light. We observe that higher values of g_1 in the second column causes a greater reduction of transmission as the influence of the qubits on generating the effective photon-photon interactions has increased, Fig. 3.1(e,f). We see that with increase in I_{in}, the valley between the peaks rises gradually until it supersedes the lowering of transmission. At this moment, the peaks disappear and we observe maximum photon blockade and reduction of transmission. At even higher intensity, Fig. 3.1(g,h), the rise of transmission at $\omega_p = \omega_a$ continues and the transmission profile starts to look a bit like the one for a single resonator. This occurs as the qubit gets saturated by photons and most incoming photons pass through the resonator and transmitted with very little influence of the qubit. Thus, there are no longer effective photon-photon interactions and related photon blockade in transmission at very high intensities.

We show the variation of transmission with intensity in Fig. 3.1(i,j). We see that the QCA has matched the photon blockade of transmission as predicted by the THLE to some extent, but the modified QCA results have matched the THLE results perfectly. We must note that any lowering of transmission in QCA is due to shifting of transmission profile and not due to

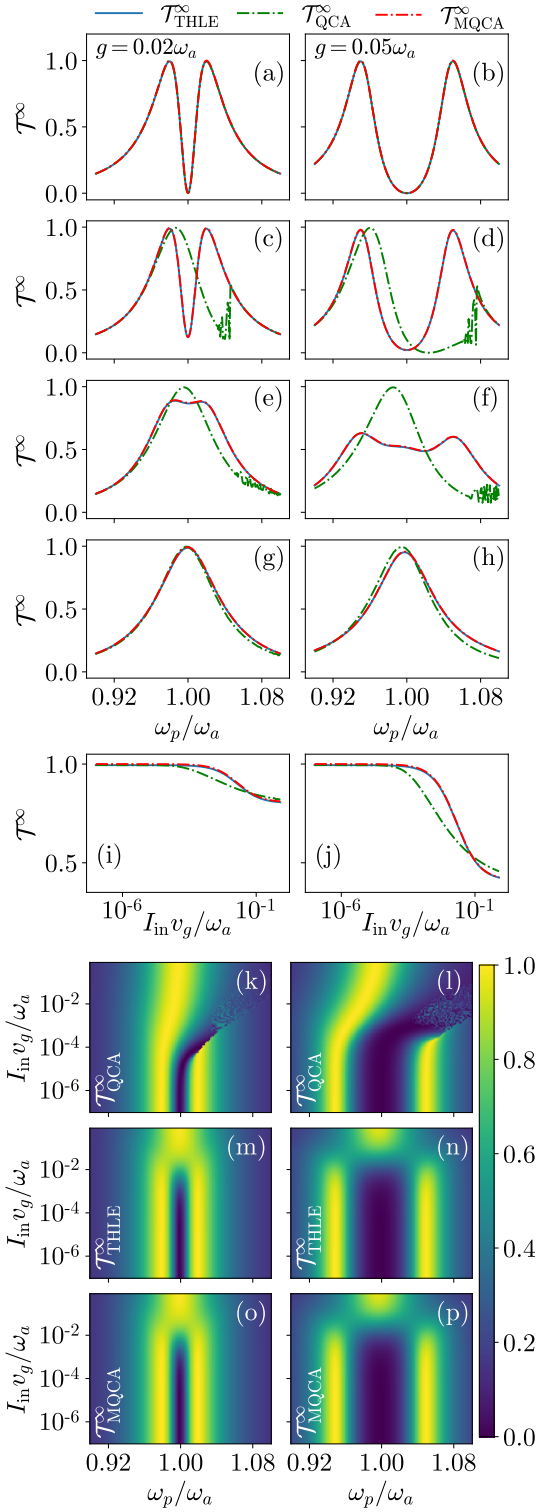

Fig. 3.1 (Caption on next page.)

Fig. 3.1 Single qubit side-coupled to a single resonator transmission results showing comparison between the THLE ($\mathscr{T}^{\infty}_{\text{THLE}}$), quasi-classical ($\mathscr{T}^{\infty}_{\text{QCA}}$) and modified QCA ($\mathscr{T}^{\infty}_{\text{MQCA}}$) analyses. The first four rows show the effect of increasing input intensity I_{in} (in terms of ω_a/v_g) as $I_{\text{in}} = 1.12\times10^{-6}$(a,b), $I_{\text{in}} = 7.1\times10^{-4}$(c,d), $I_{\text{in}} = 0.034$(e,f) and $I_{\text{in}} = 0.68$(g,h) at two different resonator-qubit coupling strengths of $g_1 = 0.02\omega_a$ and $g_1 = 0.05\omega_a$ in the two columns respectively. Change in transmission on increasing I_{in} is shown in (i,j) at, $\omega_p = 0.98\omega_a$(i) and $\omega_p = 0.95\omega_a$(j). Variation of the entire transmission profile with increasing I_{in} is shown in the last three rows for QCA, THLE and modified QCA respectively. The other parameters are: $\omega_{r_1} = \omega_{q_1} = \omega_a$, $\Gamma_L = \Gamma_R = 0.02\omega_a$ and $U = 1.05\omega_a$.

an effective photon-photon interactions. These results shows that the QCA is accurate for some parameters in the side-coupled system but not for all parameters, in particular when the transmission is low. On the other hand, for all parameters, the modified QCA has shown perfect agreement. This is further confirmed by the variation of the transmission profile with the intensity as shown in the last three rows of Fig. 3.1 for QCA, THLE and modified QCA respectively. We observe that the QCA transmission profile is shifting towards right with increasing intensity, Fig. 3.1(k,l) and shows little agreement with the THLE results at intermediate intensities. The modified QCA, however, has perfectly captured all the features predicted by the THLE analysis, Fig 3.1(m,n,o,p).

We show the transmission results for a medium of two qubits coupled to a chain of two resonators at different inter-resonator coupling strengths (J_x) and resonator-qubit coupling g_j in Fig. 3.2. Each column has constant J_x, where the first two columns have low $J_x(=\Gamma_L/2 = \Gamma_R/2)$ and the last column has high $J_x(=\Gamma_L = \Gamma_R)$. Each column also has a constant g_j with low $g_j(=0.02\omega_a)$ in the first column and high $g_j(=0.05\omega_a)$ in the last two columns. At low intensity and J_x, the transmission profile from the THLE analysis shows perfect resonant photon transport with two peaks separated by a valley with no photon transport at $\omega_p = \omega_a$, Fig. 3.2(a,b). Increasing g_j causes the resonance peaks to move away from each other, Fig. 3.2(a,b). The individual peak splits as we increase J_x which results into four peaks in the transmission profile with no transmission at $\omega_p = \omega_a$, Fig. 3.2(c).

The input intensity (I_{in}) is increased as we go down the column in the first four rows. In all cases, from the THLE analysis we observe disruption of photon transport with increase in I_{in} due to effective photon-photon interaction along with gradual increase in transmission at $\omega_p = \omega_a$. At low J_x, the photon-photon interaction causes lowering of transmission peaks, similar to the single resonator qubit pair case in Fig. 3.1, where the transmission keeps decreasing till intermediate intensities, Fig. 3.2(d,e,g,h). At even higher intensity, the qubits starts to get saturated by photons and a large photon transport is restored in the absence of inelastic scattering of the photons, Fig. 3.2(j,k). At higher J_x, we observe from the THLE

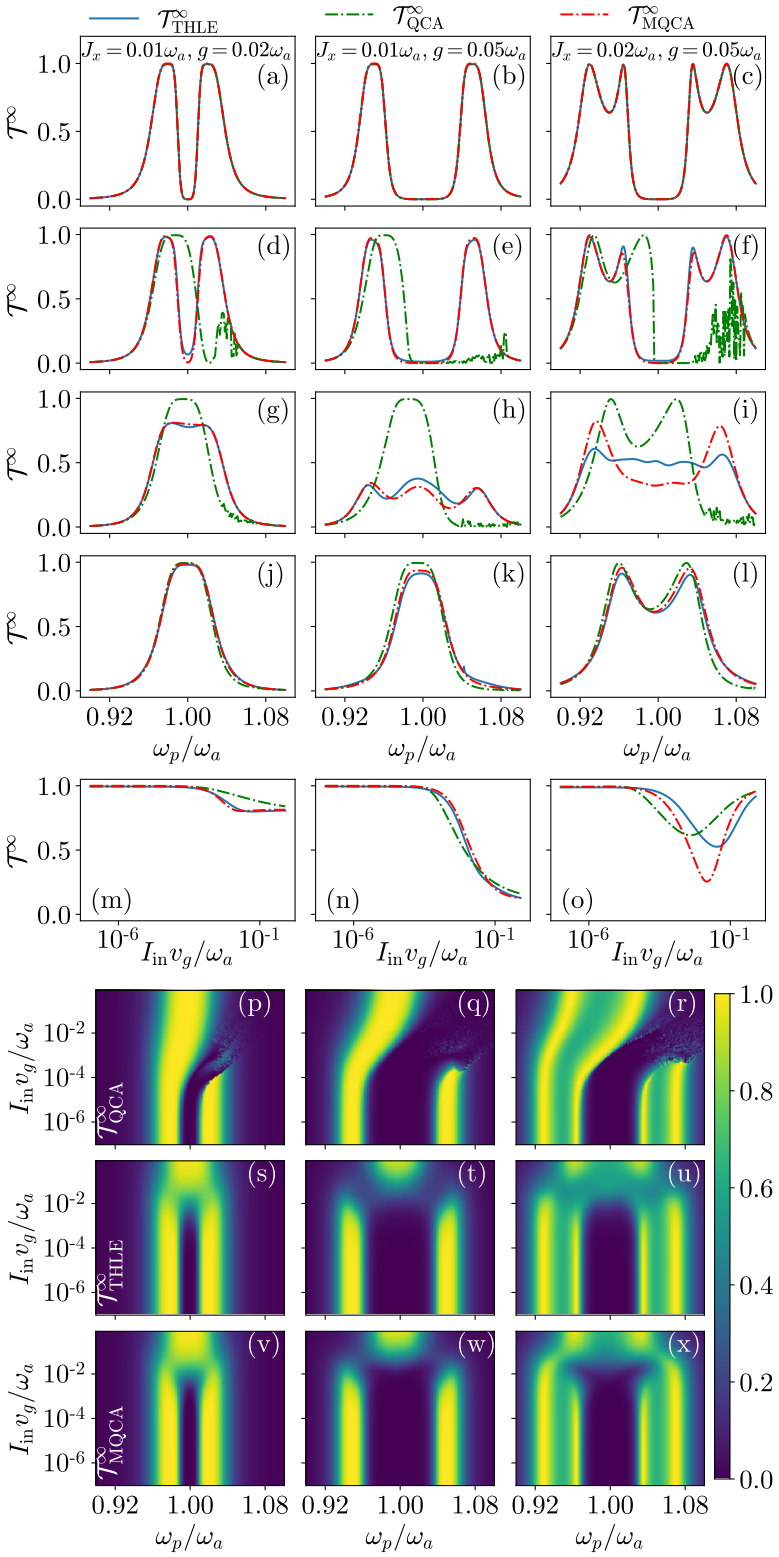

Fig. 3.2 (Caption on next page.)

Fig. 3.2 Two side-coupled qubits transmission results showing the effects of inter-resonator coupling (J_x) as well as a comparison between the THLE ($\mathscr{T}^{\infty}_{\text{THLE}}$), quasi-classical ($\mathscr{T}^{\infty}_{\text{QCA}}$) and modified QCA ($\mathscr{T}^{\infty}_{\text{MQCA}}$) analyses. The three columns have $(J_x/\omega_a, g_j/\omega_a) = (0.01, 0.02), (0.01, 0.05)$ and $(0.02, 0.05)$ respectively. The first four rows show the effect of increasing input intensity I_{in} (in terms of ω_a/v_g) as $I_{\text{in}} = 1.12 \times 10^{-6}$(a,b,c), $I_{\text{in}} = 7.1 \times 10^{-4}$(d,e,f), $I_{\text{in}} = 0.034$(g,h,i) and $I_{\text{in}} = 0.68$(j,k,l). Transmission with increasing I_{in} is shown in (m,n,o) at $\omega_p = 0.98\omega_a$(m), $\omega_p = 0.95\omega_a$(n) and $\omega_p = 0.965\omega_a$(o). Variation of the entire transmission profile with increasing I_{in} is shown in the last three rows each for QCA, THLE and modified QCA respectively. The other parameters are: $\omega_{r_j} = \omega_{q_j} = \omega_a$, $\Gamma_L = \Gamma_R = 0.02\omega_a$ and $U = 1.05\omega_a$.

analysis that out of four peaks the ones near $\omega_p = \omega_a$ lose transmission first as we increase I_{in} as shown in Fig. 3.2(f). With further increase in I_{in}, the effective photon-photon interactions and related photon blockade increase, and their effect is seen in the entire transmission profile, Fig. 3.2(i).

The overall effect of I_{in} on transmission is shown in Fig. 3.2(m,n,o), which shows reduction of transmission peak due to effective photon-photon interactions for the three analyses at various parameters. At low J_x, Fig. 3.2(m,n), reduction of transmission predicted by THLE is captured fairly accurately by the modified QCA. The QCA does not capture the reduction of transmission accurately in Fig. 3.2(m) but shows agreement at some intermediate intensities with the THLE analysis in Fig. 3.2(n). We must note that reduction of transmission in QCA is due to shifting of transmission profile and not because of photon blockade. At higher J_x, Fig. 3.2(o), modified QCA shows less accuracy in matching the lowering of transmission predicted by THLE analysis while simple QCA has even larger disagreement with THLE. We show the entire transmission profile with varying I_{in} in the last three rows of Fig. 3.2 for the QCA, THLE and modified QCA respectively. We can observe that for both values of J_x the QCA fails to match the features of THLE analysis results for a large range of parameters. The modified QCA, however, is able to capture most of the transmission features as predicted by THLE analysis. The agreement between these two analysis is good at low J_x, however, we also observe that the modified QCA becomes less accurate as J_x is increased.

We show the effects of increasing system size in the side-coupled qubits medium in Fig 3.3 where the left and right columns are for three and four qubits respectively. The first four rows correspond to increasing I_{in} in every column. The THLE truncation is increased for two system sizes in each column with $m = 4$ and $m = 2$ respectively and large U ensures the stability of transmission results. At low intensity, the side-coupled qubits medium shows perfect resonant photon transport with two major transmission peaks each having three smaller peaks for $N = 3$ near maximum transmission, Fig. 3.3(a). Larger system sizes have

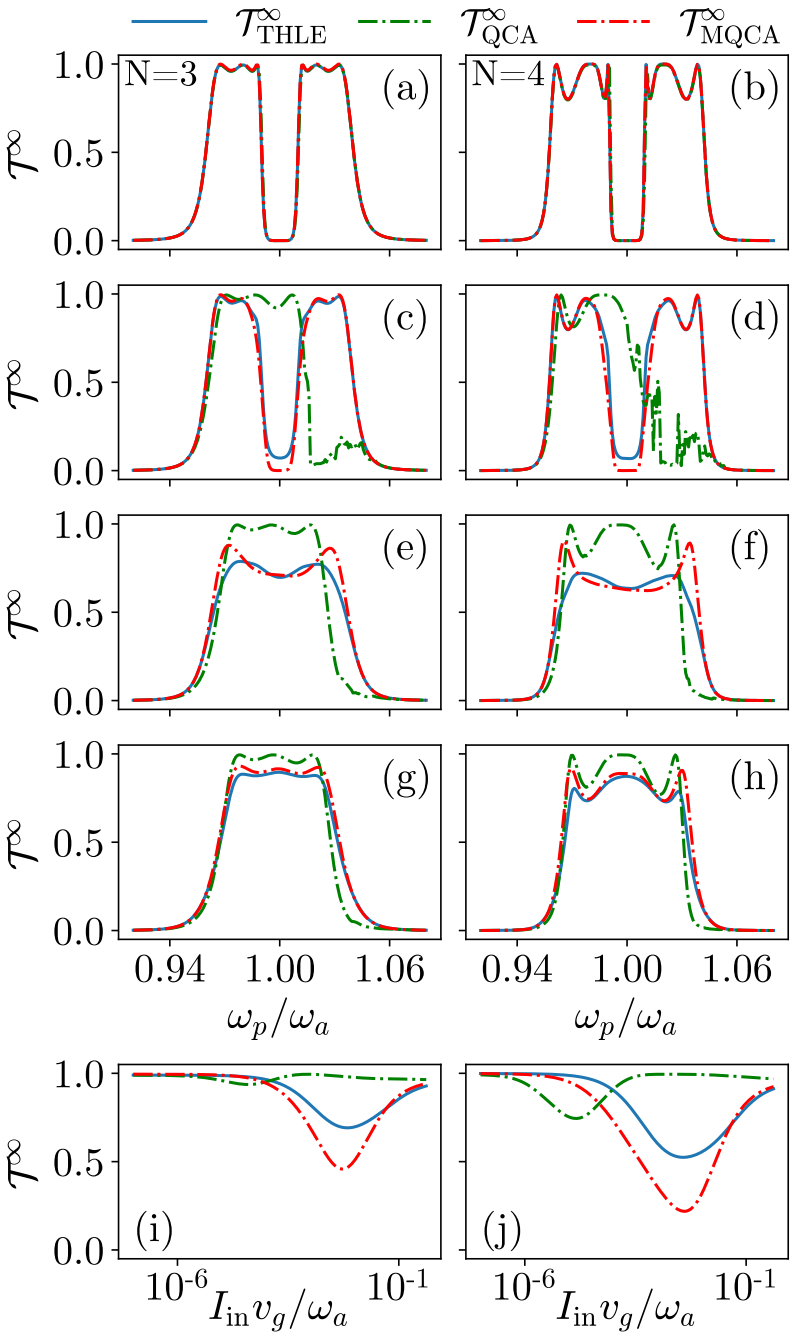

Fig. 3.3 Longer side-coupled system steady-state transmission for the THLE ($\mathscr{T}^{\infty}_{\mathrm{THLE}}$), quasi-classical ($\mathscr{T}^{\infty}_{\mathrm{QCA}}$) and modified QCA ($\mathscr{T}^{\infty}_{\mathrm{MQCA}}$) analyses. The two columns show results for system sizes (N) of 3 and 4 qubits respectively. The first four rows show transmission profiles with input intensity I_{in} (in terms of ω_a/v_g) increasing on going down the columns as $I_{\mathrm{in}} = 1.12\times10^{-6}$(a,b), $I_{\mathrm{in}} = 7.1\times10^{-4}$(c,d), $I_{\mathrm{in}} = 0.034$(e,f) and $I_{\mathrm{in}} = 0.135$(g,h). The last row shows transmission with increasing intensity for the corresponding system sizes at $\omega_p = 0.9872\omega_a$(i) and $\omega_p = 0.9896\omega_a$(j). The remaining parameters are, $\omega_{r_j} = \omega_{q_j} = \omega_a$, $\Gamma_L = \Gamma_R = 0.02\omega_a$, $J_x = 0.01\omega_a$, $g_j = 0.02\omega_a$, $U = 1.05\omega_a$.

more peaks, however, in Fig. 3.3(b) for a medium of four side-coupled qubits the middle two peaks are merged and we can only observe three peaks distinctly in each major peak. Increasing resonant peaks with system size can be observed distinctly at higher J_x. When we increase I_{in} for each system size as we go down the column, the THLE analysis shows a reduction in photon transport as well as total transmission due to the effective photon-photon interactions resulting into photon blockade at intermediate I_{in}. The peaks closer to the center show the reduction of transmission first. At even higher intensity, Fig. 3.3(g,h), the qubits start to get saturated by photons, which results in a revival of photon transport in the medium, and the transmission profile is primarily controlled by the features of the resonator chain.

We show the transmission from the three analyses with increasing I_{in} at one of the intermediate peaks ($\omega_p = 0.95\omega_a$) in the last row of Fig. 3.3. We observe interesting non-monotonic behavior similar to Fig. 3.2(m,o) showing a decrease in transmission due to effective photon-photon interaction and then a revival of photon transport through the resonator chain due to saturation of qubits by photons. The QCA fails to predict the reduction of transmission over a wide range of intensity, while the modified QCA has shown good agreement with THLE analysis in predicting this reduction.

3.3.1 Inhomogeneous side-coupled systems

Finally, in Fig. 3.4, we consider photon transport through an inhomogeneous medium of side-coupled qubits, where we introduce inhomogeneity in qubit frequencies ($\delta\omega_{q_j}$) and the qubit-resonator couplings (g_j) [Underwood et al., 2012; See et al., 2019; Orell et al., 2019]. For an inhomogeneous or disordered system, the coherent quantum behavior itself has the possibility of showing reduced transmission due to Anderson localization at low intensity as seen in Fig. 3.4(a,b). As I_{in} is increased there is an initial loss of transmission due to effective photon-photon interactions even for the inhomogeneous system, 3.4(c,d). However, at high I_{in}, photon transport re-emerges as qubits get saturated by photons and qubits have less effect on photons transiting through the resonators, Fig. 3.4(e,f). We observe that the transmission profile for both homogeneous and inhomogeneous qubits is very similar at high I_{in} as the resonators in the medium are all identical. The small difference at high I_{in} is due to non-identical qubits being at different saturation levels. The non-monotonic reduction and rise of transmission is observed in case of both homogeneous and inhomogeneous qubits as shown in Fig. 3.4(g,h). A very interesting effect is seen for the inhomogeneous system, namely, the effective photon-photon interactions end up resulting in a higher transmission than its photon transport at low intensity, which is lowered due to Anderson localization.

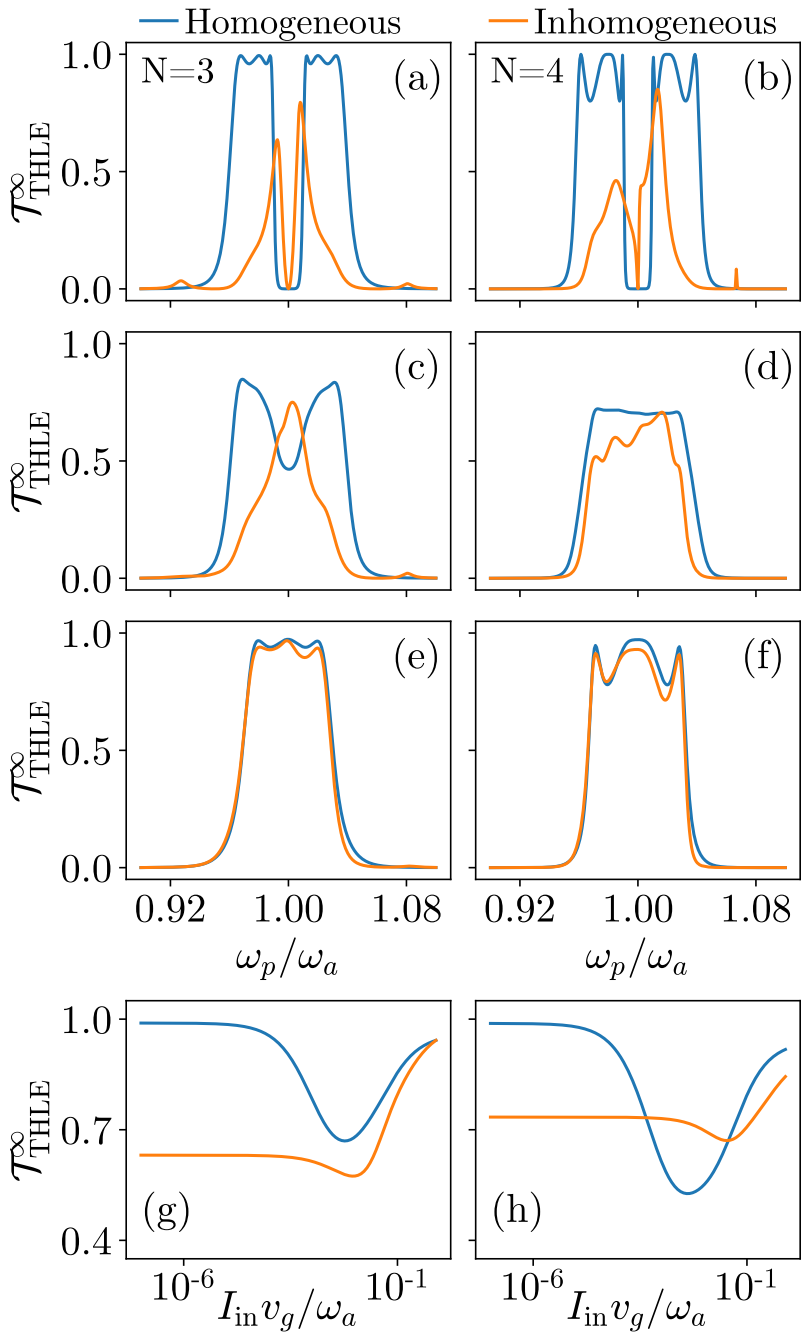

Fig. 3.4 Inhomogeneous side-coupled systems THLE transmission profile for system sizes $N = 3,4$ in the left and right columns respectively. The first three rows show transmission profiles with input intensity I_{in} (in terms of ω_a/v_g) increasing on going down the columns as $I_{\mathrm{in}} = 1.12 \times 10^{-6}$(a,b), $I_{\mathrm{in}} = 9.4 \times 10^{-3}$(c), $I_{\mathrm{in}} = 0.047$(d) and $I_{\mathrm{in}} = 0.68$(e,f). The last row shows transmission with I_{in}, for homogeneous and inhomogeneous qubits respectively, at $\omega_p = 0.988\omega_a$ and $0.992\omega_a$ for $N = 3$(g), and at $\omega_p = 1.01\omega_a$ for $N = 4$(h). For the homogeneous medium, both system sizes have $g_j = 0.02\omega_a$ and $\omega_{q_j} = \omega_a$. For the inhomogeneous system $N = 3$ has $g_j/\omega_a = (0.04, 0.01, 0.04)$, $\omega_{q_j}/\omega_a = (0.95, 1.0, 1.06)$ while $N = 4$ has, $g_j/\omega_a = (0.05, 0.007, 0.02, 0.04)$, $\omega_{q_j}/\omega_a = (0.92, 1.0, 1.06, 1.08)$. The remaining parameters are, $\omega_{r_j} = \omega_a$, $\Gamma_L = \Gamma_R = 0.02\omega_a$, $J_x = 0.01\omega_a$ and $U = 1.05\omega_a$.

3.3.2 Inelastic scattering of the photons

To investigate the elastic and inelastic components of photon transmission, we first calculate the transmission amplitude ($t_N(\omega_p)$) for each of the mediums of size N which is given by

$$t_N(\omega_p) = \frac{-2i\pi g_R}{E_p}\langle \chi_N \rangle, \tag{3.27}$$

where, χ_N is b_N for the direct-coupled qubits medium and f_N for the side-coupled qubits medium.

Interestingly, the mod-squared transmission amplitude $|t_N(\omega_p)|^2$ does not give us the total transmission probability ($\mathscr{T}_{\text{THLE}}$). It only captures what is called coherent component of transmission [Hoi et al., 2011] as opposed to an incoherent component that displays inelastic scattering of the photons at higher intensity. To investigate the coherent and incoherent contribution in the transmission probability, we compare the mod-squared transmission amplitudes ($|t_N(\omega_p)|^2$) with the transmission probability ($\mathscr{T}^{\infty}_{\text{THLE}}$), at $m = 6$, for the two mediums of size $N = 2$ in Fig. 3.5. At low light intensities, we find that $|t_2(\omega_p)|^2$ is equal to $\mathscr{T}^{\infty}_{\text{THLE}}$ in Fig. 3.5(a,b), which indicates that there is very little incoherent contribution to the transmission due to the nonlinearities at such intensities. As we increase the intensity, we find that the difference between $\mathscr{T}^{\infty}_{\text{THLE}}$ and $|t_2(\omega_p)|^2$ increases, and the coherent part $|t_2(\omega_p)|^2$ is less than the total transmission in Fig. 3.5 (c,d). The difference between $\mathscr{T}^{\infty}_{\text{THLE}}$ and $|t_2(\omega_p)|^2$ provides an estimate of incoherently transmitted photons in our mediums.

As only lossless systems have been considered here, the presence of inelastic components can be confirmed by evaluating the power spectrum of the transmitted photons. In the direct-coupled qubits, it can be obtained by [Roy, 2017]:

$$P_{tr}(\omega) = Re \int_0^{\infty} \frac{d\tau}{\pi} e^{i\omega\tau} \langle a^{\dagger}_{R_k}(t) a_{R_k}(t+\tau) \rangle. \tag{3.28}$$

Under the initial condition as mentioned earlier, the above expression reduces down to

$$P_{tr}(\omega) = \frac{2\Gamma_R}{\pi v_g} Re \int_0^{\infty} d\tau e^{i\omega\tau} \langle b^{\dagger}_N(t) b_N(t+\tau) \rangle. \tag{3.29}$$

The procedure to calculate the two-time correlation of qubit operators $\langle b^{\dagger}_N(t) b_N(t+\tau) \rangle$ for a single qubit is mentioned in [Roy, 2017]. The procedure can be extended to multiple direct-coupled qubits to evaluate the transmission power spectrum having coherent and incoherent components, i.e, $P_{tr}(\omega) = P^{coh}_{tr}(\omega) + P^{inc}_{tr}(\omega)$. For a single qubit, the coherent component is $P^{coh}_{tr}(\omega) = (2\Gamma_R/v_g)|\mathscr{S}_{01}(t \to \infty)|^2 \delta(\omega - \omega_p)$ while the incoherent component is $P^{inc}_{tr}(\omega) = (\Gamma_R/\pi) Re(I_3)$ where I_3 is given as

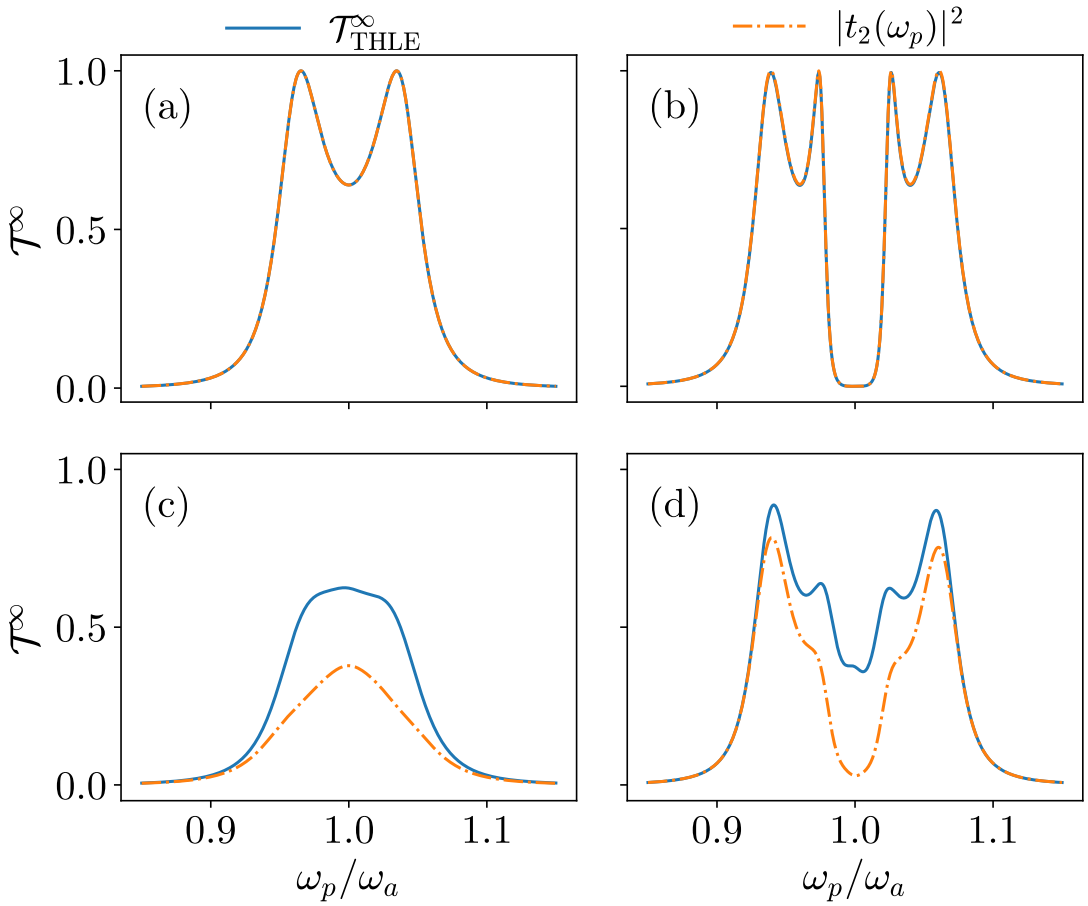

Fig. 3.5 Transmission profiles comparing the mod-square of transmission amplitude ($|t_2(\omega_p)|^2$) with transmission probabilities ($\mathcal{T}^{\infty}_{\mathrm{THLE}}$) for two ($N=2$) direct-coupled qubits (a,c) and two side-coupled qubits (b,d). The incident photon intensity I_{in} (in terms of ω_a/v_g) increases on going down the column as $I_{\mathrm{in}} = 1.0\times10^{-6}(a,b)$ and $I_{\mathrm{in}} = 0.011(c,d)$. Parameters are: $\omega_{q_j} = \omega_{r_j} = \omega_a$, $J_x = \Gamma_L = \Gamma_R = 0.02\omega_a$, $U = 1.05\omega_a$, $g_j = 0.04\omega_a$.

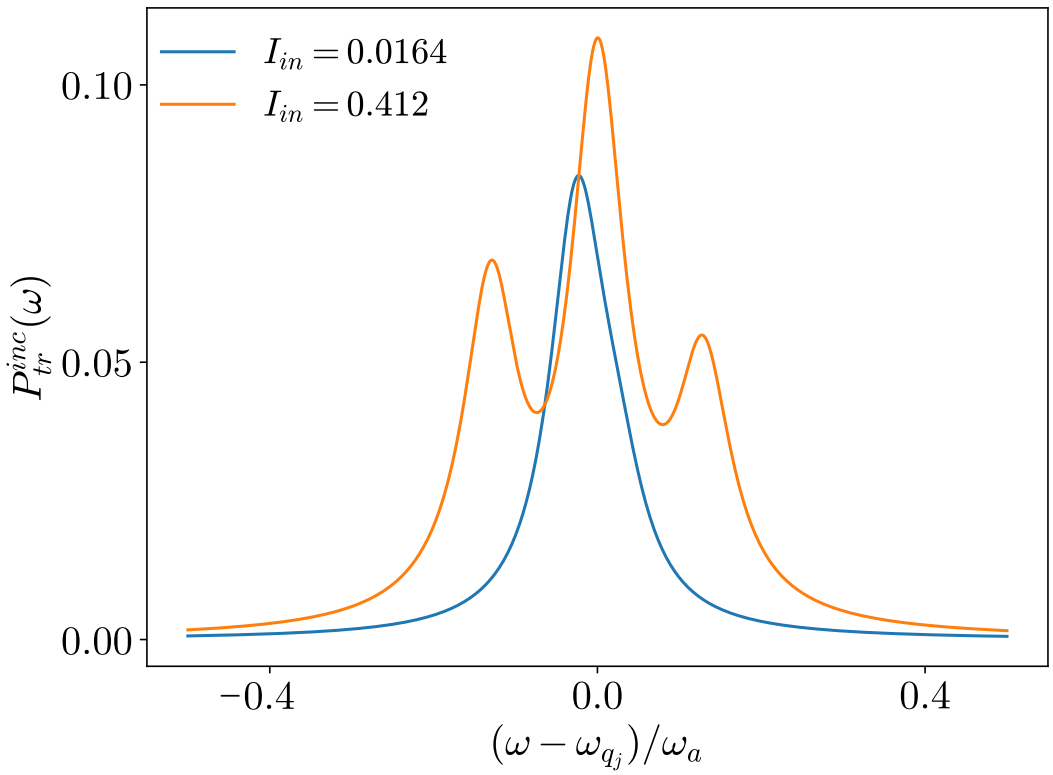

Fig. 3.6 The incoherent component of power spectrum showing inelastic scattering of photons (the two side peaks at higher intensity) for two direct-coupled qubits at resonant input frequency. Intensity (I_{in}) is in terms of ω_a/v_g. Parameters are: $\omega_{q_j} = 1.0\omega_a, J_x = \Gamma_L = \Gamma_R = 0.02\omega_a$, $U = 1.05\omega_a$.

$$I_3 = \frac{|\mathscr{S}_{01}(\infty)|^2 - \mathscr{S}_{11}(\infty)}{\mu_1} + \frac{\Omega_L^2(\mathscr{S}_{10}(\infty))^2 - \Omega_L^2(|\mathscr{S}_{01}(\infty)|^2 - \mathscr{S}_{11}(\infty))\mu_2/\mu_1 - 2i\Omega_L\mu_2\mathscr{S}_{10}(\infty)\mathscr{S}_{11}(\infty)}{2\mu_1\mu_2\mu_3 + \Omega_L^2(\mu_1+\mu_2)}, \quad (3.30)$$

where $\mu_1 = -(\Gamma_L+\Gamma_R) + i(\omega - \omega_{q_1})$, $\mu_2 = -(\Gamma_L+\Gamma_R) + i(\omega + \omega_{q_1} - 2\omega_p)$ and $\mu_3 = -(\Gamma_L+\Gamma_R) + i(\omega - \omega_p)$. The above expressions are also valid for larger system sizes and their power spectrum can be obtained by replacing the operators with the ones for the last qubit.

The incoherent part of the transmission power spectrum for two direct-coupled qubits is shown in Fig. 3.6. At low incident intensity, we observe a single peak around the qubits' frequency. However, as the incident intensity is increased, we observe three peaks. The three peaks at high input light intensity are known as the Mollow triplets. These triplets are characteristic of the inelastically scattered photons [Astafiev et al., 2010].

Further, to demonstrate that the mediums considered here are lossless, we numerically verify that the sum of steady-state reflection and transmission probabilities is unity in Fig. 3.7. This is true even at higher intensities, Fig. 3.7 (c,d), where the effects of interactions are active.

3.3.3 Single-photon transport in a side-coupled medium

To understand the single-photon transport dynamics in a single resonator-qubit pair, we first write the side-coupled qubits system's Hamiltonian given in Section 3.1 in real-space in which the momentum space operators are replaced by their Fourier transform. The real-space Hamiltonian is thus given as

$$\frac{H_r}{\hbar} = \frac{H_{side}}{\hbar} - iv_g \int dx \left(a_{Lx}^\dagger \frac{\partial}{\partial x} a_{Lx} + a_{Rx}^\dagger \frac{\partial}{\partial x} a_{Rx} \right) + \left(\sqrt{2v_g\Gamma_L} f_1^\dagger a_{L0} + \sqrt{2v_g\Gamma_R} f_1^\dagger a_{R0} + H.c. \right) \quad (3.31)$$

As before we assume a photon is incoming from the left of the medium. For the side-coupled medium of a single qubit-resonator pair in the ground state, the wave function of an incoming single photon is given by

$$|\psi\rangle_{in} = \frac{1}{\sqrt{2\pi}} \int dx e^{ikx} a_{Lx}^\dagger |\phi\rangle \otimes |0\rangle_r \otimes |0\rangle_q, \quad (3.32)$$

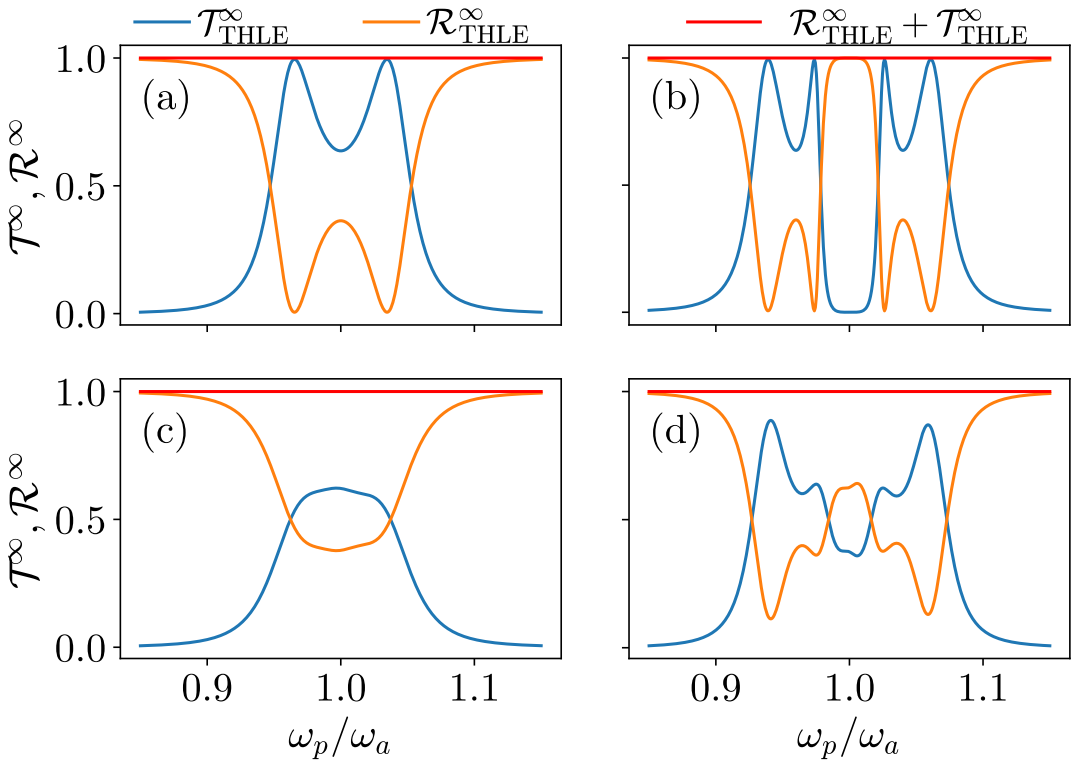

Fig. 3.7 The transmission and reflection probabilities along with their sum with increasing ω_p for a system of two direct-coupled qubits (a,c) and two side-coupled qubits (b,d). Photon intensity I_{in} (in terms of ω_a/v_g) increases on going down the column as $I_{\mathrm{in}} = 1.0\times10^{-6}(a,b)$ and $I_{\mathrm{in}} = 0.011(c,d)$. Parameters are: $\omega_{q_j} = \omega_{r_j} = \omega_a$, $J_x = \Gamma_L = \Gamma_R = 0.02\omega_a$, $U = 1.05\omega_a$, $g_j = 0.04\omega_a$.

where k is the wave vector of the incoming photon and $|\phi\rangle$ denotes the vacuum of the light field. $|0\rangle_r$ and $|0\rangle_q$ indicate the ground state of the resonator and qubit, respectively. An incoming single photon can excite the resonator and qubit to their excited state $|1\rangle_r$ and $|1\rangle_q$. Therefore, the wave function of the system after the photon interacts with the medium ($|\psi\rangle_s$) is given by

$$|\psi\rangle_s = \frac{1}{\sqrt{2\pi}} \int dx \{\delta(x)[e_k^r|\phi\rangle \otimes |1\rangle_r \otimes |0\rangle_q + e_k^q|\phi\rangle \otimes |0\rangle_r \otimes |1\rangle_q] + [\Phi_k^L(x)a_{Lx}^\dagger + \Phi_k^R(x)a_{Rx}^\dagger]|\phi\rangle \otimes |0\rangle_r \otimes |0\rangle_q\}, \tag{3.33}$$

where e_k^q and e_k^r are the amplitudes of the excited resonator and qubit, respectively. Here, $\Phi_k^L(x)$ and $\Phi_k^R(x)$ are the amplitudes of the scattered photons in the left and right sides of the side-coupled medium.

These amplitudes can be found by the time-independent Schrödinger equation $H_r|\psi\rangle_s = \hbar\omega_p|\psi\rangle_s$, which gives two coupled linear equations for the amplitudes of the resonator and the qubit, and two more inhomogeneous differential equations for the amplitudes of photons. The two differential equations are

$$-iv_g\frac{\partial}{\partial x}\Phi_k^L(x) + \sqrt{2v_g\Gamma_L}e_k^r\delta(x) = \omega_p\Phi_k^L(x), \tag{3.34}$$

$$-iv_g\frac{\partial}{\partial x}\Phi_k^R(x) + \sqrt{2v_g\Gamma_R}e_k^r\delta(x) = \omega_p\Phi_k^R(x). \tag{3.35}$$

By following [Manasi and Roy, 2018], the Eqs. 3.34 and 3.35 are regularized (at $x = 0$) and we assume photon coming from the left of the medium which gives

$$\Phi_k^L(0) = 1 - i\sqrt{\frac{\Gamma_L}{2v_g}}e_k^r, \tag{3.36}$$

$$\Phi_k^R(0) = -i\sqrt{\frac{\Gamma_R}{2v_g}}e_k^r. \tag{3.37}$$

The initial states eq. 3.36 and 3.37 are then substituted in the solutions of the medium elements. Therefore, we are left with the equations of resonator and qubit amplitudes which are written as

$$(\omega_{r_1} - \omega_p - i(\Gamma_L + \Gamma_R))e_k^r + g_1e_k^q = -\sqrt{2v_g\Gamma_L}, \tag{3.38}$$

$$(\omega_{q_1} - \omega_p)e_k^q + g_1e_k^r = 0. \tag{3.39}$$

The transmission amplitude for this medium is given by

$$t_1^s(\omega_p) = -i\sqrt{\frac{2\Gamma_R}{v_g}}e_k^r. \tag{3.40}$$

By using the solutions of Eq. 3.38 and 3.39, we obtain the transmission amplitude for a single-site side-coupled qubit medium $t_1^s(\omega_p)$ as

$$t_1^s(\omega_p) = \frac{2i\sqrt{\Gamma_L\Gamma_R}(\omega_{q_1} - \omega_p)}{(\omega_{r_1} - \omega_p - i(\Gamma_L + \Gamma_R))(\omega_{q_1} - \omega_p) - g_1^2}. \tag{3.41}$$

The numerator of Eq. 3.41 explains the complete reduction of transmission at resonance with the qubit. The mod-squared transmission amplitude for the qubit-resonator pair $|t_1^s(\omega_p)|^2$ shows two peaks at the photon frequencies

$$\omega_{p_\pm} = \left(\frac{\omega_{r_1} + \omega_{q_1}}{2}\right) \pm \sqrt{\left(\frac{\omega_{r_1} - \omega_{q_1}}{2}\right)^2 + g_1^2}. \tag{3.42}$$

3.4 Conclusion

In this chapter, we have continued the approach of the previous chapter to explore the transmission properties of photons through a lattice of side-coupled qubits, where the qubits have on-site interaction. With the increase in intensity of incoming photons in a coherent state, this lattice also develops effective photon-photon interactions and related photon blockade mediated by the on-site interaction at the qubits. The side-coupled qubits, at low intensity, also show resonance peaks with maximum transmission and a transmission minima at the qubit frequency. With an increase in intensity, the resonance peaks lowers due to photon blockade along with rise in transmission at the qubit frequency. At a very high intensity the qubits get saturated and their effects start to disappear resulting in a revival of photon transport for the side-coupled case. A non-monotonic behavior of transmission with increase in I_{in} is observed for both homogeneous and inhomogeneous side-coupled qubits.

We performed a quasi-classical analysis (QCA) for the side-coupled lattices also, which again completely fails to show any transmission reduction due to photon blockade. For this lattice also, the QCA shows agreement with truncated Heisenberg-Langevin equation (THLE) at single particle limit but fails at higher intensities and shows a shift in the QCA transmission profile. We were again able to modify the QCA equations by introducing a complex on-site interaction by matching the THLE and QCA transmissions for the single site case.

The modified QCA, again, shows perfect agreement with THLE results for all input intensity values fairly accurately at low coupling between the resonators (J_x) which is not surprising as the correction was derived from the THLE for single resonator qubit pair with enough truncation to capture the photon blockade and saturation phenomena. Unlike the direct coupled case, for this lattice, at very high intensities we essentially observe transmission through a harmonic chain of resonators with little effects from the qubits. In this limit, the qubits can be thought of as additional baths, and the photon transport is mainly by the resonator chain. However, with increase in J_x, the effectiveness of modified QCA reduces. We hope that further studies will provide more insight into improving this approach to work for an even wider set of parameters.